PAPER

Templated synthesis of multi-hierarchical layered double hydroxide microspheres†

Tomasz Kondratowicz, [a] Cyril Besnard, [b] Zoë Turner, [a] Jin-Chong Tan, [b] Chunping Chen, *[a] Roland Turnell-Ritson [a] and Dermot O'Hare *[a]

Herein, we report a green, scalable and cost-effective synthesis of microspherical Mg/Al–CO$_3$ LDHs with an average particle size and size distribution of 34 ± 6 μm with a multi-hierarchical morphology. The microspheres are composed of crystalline 300 nm thick Mg$_{2.25\pm0.025}$Al–CO$_3$ LDH platelets that are radially oriented into a hierarchical spherical motif. The LDH microspheres were synthesised via a hydrothermal reaction of NaAlO$_2$ with flower-like MgO microspheres which serve as both a structural template and a magnesium source. Our optimised synthesis conditions allow a uniformly dispersed phase pure LDH formation within 2 h at 80 °C. Comprehensive characterisation, including XRD, FT-IR, TGA, FIB-SEM, N$_2$ adsorption–desorption measurement, and CO$_2$-TPD, revealed that the obtained LDH microspheres exhibit a high specific surface area, total pore volume and basicity number. Our time-resolved studies provided further insights into the kinetics, structure evolution and crystallinity changes during the transformation process. These multi-hierarchical LDH microspheres can be calcined to produce multi-hierarchical layered double oxide (LDO) microspheres that demonstrate an exceptional CO$_2$ capture performance of 0.95 mmol g^{-1} (1 atm, 40 °C) and an adsorption capacity 2.8 times higher than that of flower-like MgO and 32 times higher than that of commercial MgO. This study highlights the potential for an atom-efficient templated synthesis of multi-hierarchical, porous LDH microspheres and their application in catalysis and sorption.

Introduction

Layered double hydroxides (LDHs) are typical 2D anionic layered materials with a general formula $[M^{z+}_{1-x}M'^{y+}_x(OH)_2]^{a+}[(A^{n-})_{a/n}]\cdot mH_2O$, where M^{z+} represent monovalent or divalent ($z = 1, 2$) cations and M'^{y+} are either trivalent or tetravalent ($y = 3, 4$) cations, respectively. The interlayer anions (A^{n-}) balance the net positive charge on the metal hydroxide layers (a), while intercalated water molecules establish a strong hydrogen-bonding network with the hydroxyl groups of the cationic layers and the interlayer anions. For MgAl-based LDHs ($x = a$), x is typically in the range of 0.18–0.33 giving an Mg : Al ratio $(1 - x/x)$ in the range of 2–4.6.[1,2] LDHs are highly versatile materials, allowing for precise control over their composition, structure, and properties such as high anion exchange capacity, tunable surface functionality, and good biocompatibility. In addition, LDHs can be transformed into layered double oxides (LDOs) through thermal treatment under

mild conditions (300–750 °C).[3–5] The resulting LDOs exhibit a uniform dispersion of mixed metal oxides, and demonstrate excellent structure re-construction capabilities in the presence of water and anions. As a result, both LDHs and LDOs have garnered significant attention in the fields of catalysis, environment remediation, energy storage, pharmaceutical storage and delivery, and materials science.[6–10]

LDHs can be synthesised through various methods, including co-precipitation, hydrothermal synthesis and sol–gel processes.[11] However, LDH particles obtained via these traditional approaches often suffer from aggregation after drying due to the strong hydrogen bonding between surface bound and intercalated water molecules, metal hydroxide layers, and interlayer anions. This aggregation frequently results in dense, stone-like aggregates with low surface area and limited accessibility of active metal sites, which significantly restricts their potential applications. While hydrothermal synthesis can sometimes yield individual LDH particles, the resulting platelets are typically large and/or thick platelets with limited surface area. To address these challenges, in 2013 the O'Hare group introduced a novel technique known as AMOST (Aqueous Miscible Organic Solvent Treatment).[12] This method involves dispersing the freshly co-precipitated, wet LDH cake into an aqueous miscible organic solvent which displaces bound and intercalated water, thus weakening the hydrogen-bonding

[a]Chemistry Research Laboratory, Department of Chemistry, University of Oxford, 12 Mansfield Road, Oxford, OX1 3TA, UK. E-mail: chunping.chen@chem.ox.ac.uk; dermot.ohare@chem.ox.ac.uk; Tel: +44(0)1865 272686

[b]Multifunctional Materials & Composites (MMC) Laboratory, Department of Engineering Science, University of Oxford, Parks Road, Oxford, OX1 3PJ, UK

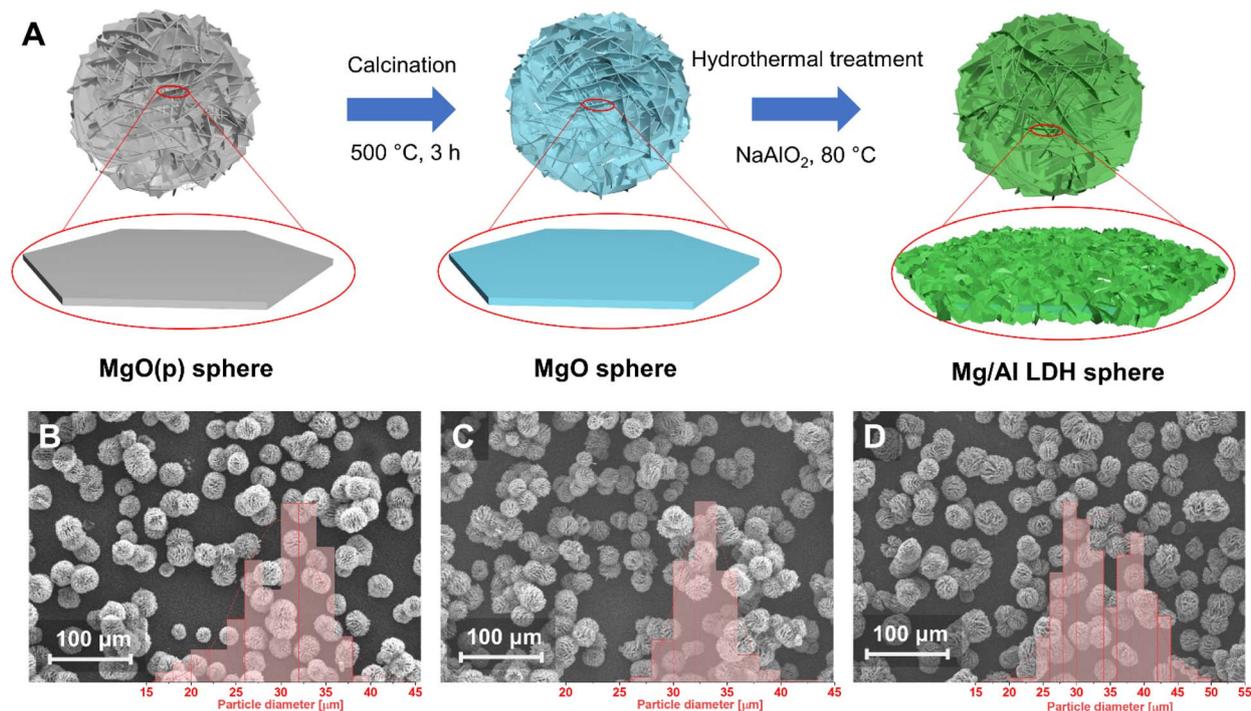† Electronic supplementary information (ESI) available. See DOI: https://doi.org/10.1039/d5ta01511a

Fig. 1 (A) Schematic illustration of the synthesis of multi-hierarchical Mg/Al–CO$_3$ LDH microspheres. (B) SEM images of MgO(p) precursor spheres, (C) MgO spheres and (D) MgAl(4 h_0.2) spheres (insets show the particle size distribution of the corresponding spheres measured from more than 200 particles in the SEM images by ImageJ software).

network. Consequently, the resulting LDHs, referred to as AMO-LDHs exhibit substantially higher surface areas (up to 500 m^2 g^{-1}) and enhanced dispersibility in non-polar hydrocarbon systems.[13–15] An alternative strategy to prevent aggregation involves immobilising LDH particles onto a support, such as SiO$_2$, zeolite, alumina, MOF, carbon, or Fe$_3$O$_4$ *via in situ* precipitation.[16–20] For instance, LDH platelets can be grown vertically from the surface of silica nanoparticles to form SiO$_2$@LDH core–shell nanosphere structures.[21] LDHs can also form hierarchical hollow structures by *in situ* dissolution of a MOF core material or post-removal of the core materials (silica and carbon).[19,22,23] While these core–shell approaches allow for tuning properties by varying the LDH composition, synthesis conditions, and core material characteristics (*e.g.*, porosity of SiO$_2$ and acidity of zeolite), they often require specialised core materials as additional components, introducing extra complexity and costs and the potential for forming undesired additional phases during these syntheses. Self-assembly of LDH platelets into 3D structures presents another promising approach to reduce aggregation while avoiding the introduction of additional materials. This typically involves using structure-directing agents such as sodium dodecyl sulfonate,[24] ammonium fluoride[25] or ethylene glycol.[26] Post-treatment normally is required to obtain pure LDH materials. The LDH materials obtained from these approaches often have particle sizes below the micrometre scale, posing challenges for industrial-scale production and practical applications.

Herein, we present a green, scalable and cost-effective strategy for synthesising LDH microspheres with multi-hierarchical structures. This approach utilises flower-like MgO microspheres both as a template and a magnesium source for Mg/Al–CO$_3$ LDH formation. The resulting Mg/Al–CO$_3$ LDH microspheres feature interconnected smaller nanoplatelets anchored onto larger platelets within a hierarchical microsphere structure (Fig. 1A). This innovative method yields highly crystalline, phase-pure MgAl–CO$_3$ LDH microspheres with uniform, monodisperse flower-like morphology, mitigates platelet aggregation, and enhances accessibility to active sites, offering a promising pathway for practical and industrial-scale applications. The closed-loop recycling of reagents and operation under mild hydrothermal conditions make it sustainable and amenable to scale up.

Results and discussion

A microspherical MgO precursor (MgO(p)) was initially synthesised *via* a modified co-precipitation[27] in water by mixing MgCl$_2$ and Na$_2$CO$_3$ followed by aging at 80 °C for 2 h. Calcination of MgO(p) at 500 °C for 3 h yields MgO microspheres which were hydrothermally reacted with NaAlO$_2$ in an aqueous solution at 80 °C (Fig. 1A). The obtained LDH samples were denoted as MgAl(x_y), where x is the synthesis time and y is the input ratio of Mg : Al.

As shown in Fig. 1B, the MgO(p) sample exhibits a very uniform, monodispersed flower-like microsphere morphology with an average particle size and size distribution of 30 ± 4.5 μm. Upon calcination at 500 °C, the morphology remains unchanged, while the particle size and size distribution slightly

increase to 33 ± 2.4 μm (Fig. 1C). Remarkably, after the hydrothermal reaction, MgAl(4 h_0.2) retains the same uniform mono-dispersed flower-like microsphere morphology with an average particle size and size distribution of 34 ± 5.6 μm (Fig. 1D). Similar methods using MgO and NaAlO$_2$ have also been reported for synthesising pure-phase LDHs.[28] The resulting LDHs typically exhibit aggregated morphologies significantly different from that of MgO. Furthermore, no free LDH particles were observed throughout the sample by SEM analysis (Fig. 1B and C), highlighting the high efficiency of the proposed top-otactic templating method for preserving the spherical MgO morphology during the conversion to an Mg/Al–CO$_3$ LDH.

The powder X-ray diffraction (XRD) pattern (Fig. 2A) reveals that MgO(p) exhibits a series of Bragg reflections from hydrated magnesium carbonate (HMC) phases, specifically the hydromagnesite group of compounds with the general formula $Mg_5(CO_3)_4(OH)_2 \cdot nH_2O$. The two prominent Bragg reflections at $2\theta = 5.7°$ and $8.7°$ confirm that the major phase present is dypingite (PDF#23-1218), that typically contains five water molecules per formula unit.[29] However, variations in hydration states, such as $Mg_5(CO_3)_4(OH)_2 \cdot 6H_2O$ and $Mg_5(CO_3)_4(-OH)_2 \cdot 8H_2O$ are also occasionally reported.[30,31] The possibility of co-existing hydromagnesite phases cannot be ruled out due to structural similarities, which may stem from different arrangements of the MgO$_6$ layers and carbonate groups parallel to the (100) plane.[32,33] To determine the precise formula of the synthesised dypingite, thermogravimetric analysis (TGA) and quantitative analysis of the elemental composition using elemental microanalysis (CHN) and inductively coupled plasma optical emission spectroscopy (ICP-OES) were conducted. As shown in Fig. 2B, MgO(p) undergoes a multi-phase decomposition process upon heating. The first weight loss of 18.62 wt%

below 300 °C corresponds to the removal of crystal water molecules from the dypingite structure, consistent with the theoretical five water molecules in dypingite. Further heating leads to dehydroxylation and decarbonation, resulting in a further 39.71 wt% weight loss. The total weight loss of 58.33 wt% closely matches the theoretical value of 58.51 wt% for the thermal decomposition of dypingite $(Mg_5(CO_3)_4(OH)_2 \cdot 5H_2O)$ to MgO. The CHN and ICP results (Table S1†) further confirm that the synthesised MgO(p) primarily comprises dypingite with a refined formula of $Mg_{5.0}(CO_3)_{4.1}(OH)_{1.8} \cdot (H_2O)_5$.

After calcination at 500 °C, the XRD pattern (Fig. 2A) confirms the formation of MgO, indicated by three characteristic reflections at $2\theta = 36.7°$, $42.7°$ and $62.0°$ corresponding to the (111), (200) and (220) reflections characteristic of periclase which has a cubic lattice ($Fm3m$ space group). The average of the a-lattice parameter and crystallite size of MgO were calculated to be 4.24 ± 0.01 Å (slightly higher than the commonly reported value of 4.21 Å[34]) and 8.7 ± 0.4 nm, respectively. Following a hydrothermal reaction for 4 h, all characteristic MgO reflections are absent and a new set of Bragg reflections are observed at $2\theta = 11.5°$, $23.2°$, $34.8°$, $39.4°$, $46.8°$, $60.8°$ and $62.1°$. These reflections could be assigned to the (003), (006), (009), 015), (018), (110) and (113) planes, respectively, typical for the rhombohedral LDH structure with a trigonal $R\bar{3}m$ space group.[22] The a and c-lattice parameters ($a = 2d_{110}$) and ($c = 3d_{003}$) were determined to be 0.305 nm and 2.310 nm, respectively, giving a d_{003} basal plane spacing of 0.770 nm. These values are consistent with the Mg$_x$Al–CO$_3$ LDH phases, featuring a Mg : Al ratio of approximately 2 and CO$_3{}^{2-}$ as the interlayer charge compensating anion as previously reported.[35,36]

Fourier transform infrared spectroscopy (FT-IR) was employed to further study the formation of these phases. As
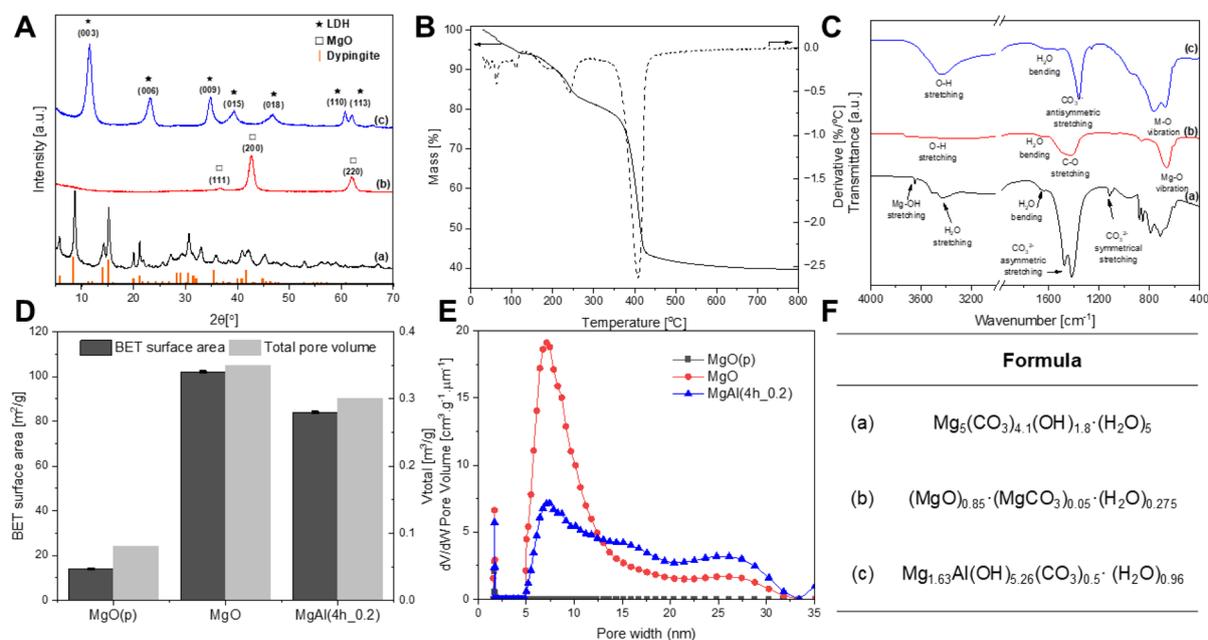

Fig. 2 (A) XRD patterns; (B) TGA and DTG profiles of MgO(p), solid and dashed line, respectively; (C) FTIR spectra; (D) BET specific surface area and total pore volume; (E) pore size distributions and (F) formula of (a) MgO(p), (b) MgO and (c) MgAl(4 h_0.2).

shown in Fig. 2C(a), MgO(p) displays characteristic absorbances of dypingite including ν(Mg–OH) stretching (3644 cm^{-1}), H$_2$O stretching (3300–3600 cm^{-1}) and bending (3648 cm^{-1}), CO$_3^{2-}$ asymmetric stretching (1416, 1473 cm^{-1}) and symmetrical stretching (1120 cm^{-1}). After calcination at 500 °C, the Mg–OH stretching and CO$_3^{2-}$ symmetrical stretching absorbances disappear while a distinct new absorbance is observed at *ca.* 660 cm^{-1}, corresponding to the Mg–O vibration, confirming the formation of MgO (Fig. 2C(b)). A broad and weak CO$_3^{2-}$ asymmetric stretching band at around (1400–1500 cm^{-1}) is still observed, that we assigned to trace amounts of residual carbonate from incomplete calcination. This is consistent with the CHN and ICP-OES data (Table S1†) which provide the formula of (MgO)$_{0.85}$·(MgCO$_3$)$_{0.05}$·(H$_2$O)$_{0.275}$. The FT-IR spectrum in Fig. 2C(c) displays a set of characteristic absorbances of hydrotalcite-like materials,[37] such as M–O vibrations (Al–O and Mg–O stretching at 760 cm^{-1} and 675 cm^{-1}, respectively), O–H stretching at 3440 cm^{-1}, water bending vibration at 1637 cm^{-1} and an intense adsorption band at 1360 cm^{-1}, associated with the ν_3 mode of CO$_3^{2-}$. This confirms the presence of carbonate in the MgAl(4 h_0.2) sample, and we note that no carbonate precursor was used in the synthesis. This is likely to originate from the residual carbonate in MgO and/or absorption of atmospheric CO$_2$ into the basic solution during the synthesis. Additionally, no other bands indicative of impurities, *i.e.* Mg(OH)$_2$ (*ca.* 3644 cm^{-1}), AlOOH (*ca.* 1097 cm^{-1}) and Al(OH)$_3$ (*ca.* 1025 cm^{-1}) are observed, which aligns with the XRD data (Fig. 2A(c)). CHN and ICP-OES (Table S1†) confirm the chemical formula of MgAl(4 h_0.2) as [Mg$_{1.63}$Al(OH)$_{5.26}$](CO$_3$)$_{0.50}$ · 0.96H$_2$O.

N$_2$ Brunauer–Emmett–Teller (BET) adsorption/desorption measurements were used to investigate the surface structure and porosity properties of these materials. As shown in Fig. S1.† all the adsorption–desorption isotherms exhibit type II behaviour with a characteristic H3 hysteresis loop, typical of plate-like particles according to the IUPAC classification.[38] The MgO(p) precursor exhibits minimal N$_2$ adsorption and the smallest hysteresis loop, indicating a non-porous structure with a low surface area. As shown in Fig. 2D, the N$_2$ BET specific surface area (S_{BET}) and total pore volume (V_{total}) for MgO(p) were determined to be 14 m^2 g^{-1} and 0.08 cm^3 g^{-1}, respectively. These values significantly increase to 101 m^2 g^{-1} and 0.34 cm^3 g^{-1}, respectively, after calcination at 500 °C. Notably, both values are significantly higher than those of commercial MgO (*i.e.* 26 m^2 g^{-1} and 0.10 cm^3 g^{-1}) (Table S2†). Following conversion to the Mg/Al–CO$_3$ LDHs both the S_{BET} and V_{total} decrease slightly to 84 m^2 g^{-1} and 0.30 cm^3 g^{-1}, respectively, probably due to the pore blockage by the formation of small LDH platelets. These trends are consistent with the pore size distribution calculated by density functional theory (DFT) (Fig. 2E). The MgO(p) precursor is largely non-porous, with only 1.7 nm pores observed. In contrast, the calcined MgO microspheres exhibit an additional pore volume with peaks in the pore size distribution at 7 nm and a broad shoulder at *ca.* 26 nm which could be ascribed to the spaces between interconnected platelets within the microspheres. This behaviour has been previously reported, and can be explained by the loss of CO$_2$

from the precursor material, leaving larger voids in the resultant MgO.[27] For MgAl(4 h_0.2), we observe in the pore size distribution a slight reduction in the number of 7 nm pores, new larger 15 nm pores and a new significant broad feature at around 26 nm, likely due to the formation of a new microtexture within the LDH microspheres.

The internal structure of these materials was further analysed using Focused Ion Beam Scanning Electron Microscopy (FIB-SEM).[39] The cross-sectional images are shown in Fig. 3. The results reveal that the flower-like MgO microspheres are composed of numerous radially oriented platelets originating from the centre and extending outward (Fig. 3A–C). The platelets are smooth, thin, and have an average thickness of approximately 100 nm as shown in in Fig. 3C. There are some previous reports on the synthesis of MgO microspheres using methods such as water-in-oil emulsion techniques,[40] and the resulting particles often present as large agglomerates composed of individual nest-like particles. After transformation into the Mg$_x$Al–CO$_3$ LDHs, the overall hierarchical features (flower-like microspheres constructed from radially arranged platelets) are preserved. Interestingly, the platelets become three times thicker (300 nm) than those observed in the MgO precursor. Moreover, the 300 nm platelets are all composed of numerous nanoplatelets that grow vertically on each side of the platelets, creating a secondary hierarchical structure (Fig. 3D–F). The energy-dispersive X-ray (EDX) mappings confirm the uniform distribution of Mg, Al and O across the entire cross-section, indicating that the Mg/Al–CO$_3$ LDH phase is formed uniformly throughout the entire microsphere, rather than being restricted to the surface of MgO.

A kinetic study of LDH formation from MgO at 80 °C was conducted by quenching the reaction at different time points.
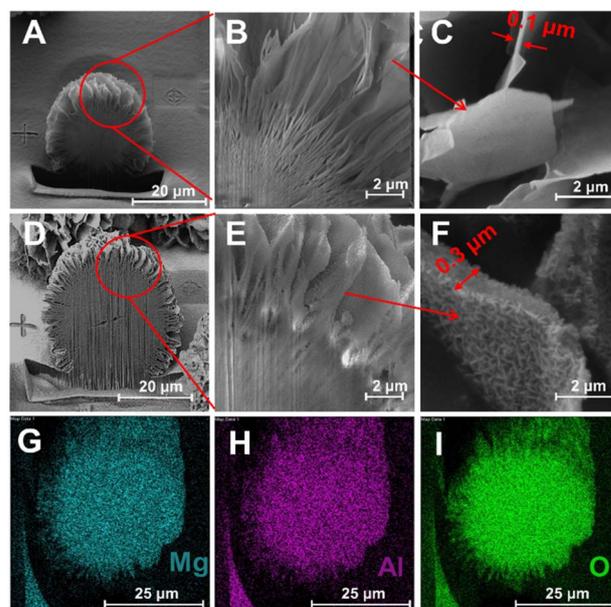

Fig. 3 (A–C) Cross sectional FIB-SEM images of MgO; (D–F) FIB-SEM images of MgAl(4 h_0.2); (G–I) cross-section EDX mapping of MgAl(4 h_0.2).

The XRD data (Fig. 4A and S2†) confirm that $Mg_xAl–CO_3$ LDHs begin to form within 15 minutes, as evidenced by the appearance of their characteristic Bragg reflections. However, the MgO Bragg reflections are still observed, indicating that the reaction is not complete at this early stage. The SEM image in Fig. 4B reveals that the small platelets (around 50 nm in diameter and 10 nm thickness) grow vertically on the large platelets after just 15 minutes. Additionally, the EDX mapping (Fig. S3†) on the cross-section of MgAl(15 min_0.2) microspheres reveals a uniform distribution of aluminium throughout the spherical structure, suggesting that aluminium is readily absorbed onto the surface of MgO. With increasing reaction time, the intensity of $Mg/Al–CO_3$ LDH Bragg reflections increases, while the MgO reflections diminish and ultimately disappear after 2 h, confirming the complete transformation of MgO into $Mg/Al–CO_3$ LDHs. The a-lattice parameter (Fig. 4C) of the $Mg/Al–CO_3$ LDHs increases from 0.303 to 0.305 nm within the first hour and then remains at 0.305 nm, indicating rapid incorporation of aluminium into the LDH structure. A linear relationship between the a-lattice parameter of the LDH $vs.$ the Mg : Al ratio has been reported in the literature.[41] Using the XRD data we determined the Mg : Al ratio in the sample ranges between 2.19–2.38, and not surprisingly this is the most common Mg : Al ratio for stable MgAl-containing LDH phases. The c-lattice parameter decreases progressively with reaction time, from 2.329 nm (MgAl(15 min_0.2)) to 2.290 nm (MgAl(48 h_0.2)), reflecting the presence of carbonate anions in the interlayer galleries, and this interlayer spacing has been proposed to result from carbonate re-orientation at extended reaction times[42] (Table S3†). The

presence of carbonate was further supported by the FT-IR spectra (Fig. S4†) where the C–O stretching absorbance became sharper and more intense as a function of reaction time. The crystalline domain lengths along the platelet stacking, c-direction ($D_{(003)}$) and in plane ab-direction ($D_{(110)}$) were calculated using the Scherrer equation (Fig. 4D). The crystallinity (crystalline domain lengths) of the LDH improves with increasing reaction time, with $D_{(003)}$ and $D_{(110)}$ increasing from 4.1 to 10.8 nm and from 4.6 to 23.1 nm, respectively, from 15 minutes to 48 h. The Mg : Al ratio in the sample was measured using ICP-OES as shown in Fig. 4D. It shows a rapid decrease in the Mg : Al ratio, from 6.95 to 1.76 in the first 2 h of reaction, indicating the rapid incorporation of aluminium into the LDH structure. This aligns with observed morphological and crystallographic changes. The N_2 adsorption–desorption isotherms for all samples retain the type II shape with H3 hysteresis loops, characteristic for plate-like particles (Fig. S5†). However, differences in total adsorption volumes were observed, affecting the BET specific surface area and the total pore volume as shown in Fig. 4F. Generally, a progressive increase of S_{BET} and V_{total} values is observed with increasing reaction time. At short reaction times (up to 1 h), both values increase rapidly from 34 to 78 $m^2 g^{-1}$ and 0.15 to 0.27 $cm^3 g^{-1}$, respectively. Between 1–4 hours, these values plateau, with S_{BET} in the range of 78–84 $m^2 g^{-1}$ and V_{total} between 0.27–0.31 $cm^3 g^{-1}$. Prolonged reaction times (24–48 h) resulted in further increases, with S_{BET} and V_{total} reaching 92–97 $m^2 g^{-1}$ and 0.44–0.45 $cm^3 g^{-1}$, respectively, despite high crystallinity of the formed $Mg/Al–CO_3$ LDHs (Fig. S2†). This is probably due to
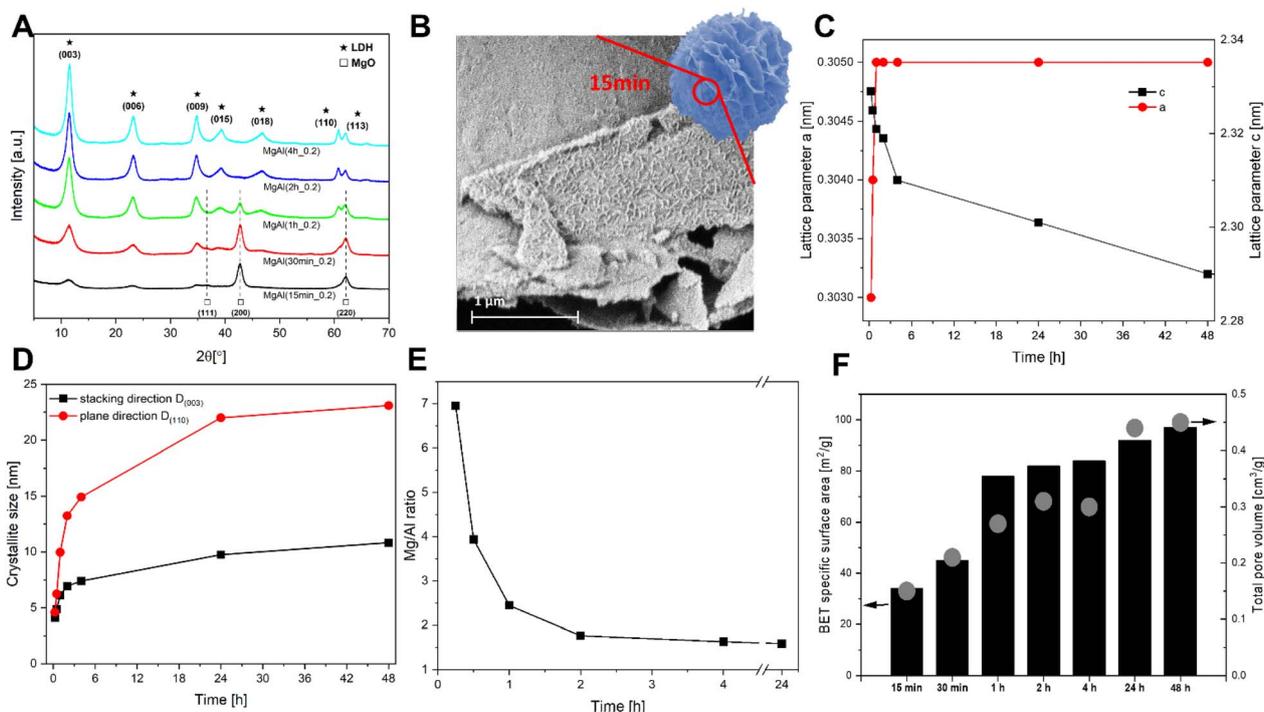

Fig. 4 A kinetic study of LDH formation from MgO microspheres at 80 °C as a function of time with Mg : Al ratio = 0.2. (A) XRD data, (B) SEM image of LDH platelets on MgAl(15 min_0.2), (C) lattice parameters, (D) crystalline domain length, (E) Mg : Al ratio, and (F) BET specific surface area and total pore volume.

Ostwald ripening where dissolution and recrystallisation processes enhance surface areas and pore volumes while improving crystallinity. Similar phenomena have been reported in the literature.[18,43]

In these syntheses, a high concentration of $NaAlO_2$ (0.35 M) was used as the aluminium source, yielding a reaction mixture with an overall Mg : Al ratio of 0.2. This represents a significant excess compared to the theoretical stoichiometric requirement to form a prototypical Mg_2Al-LDH. As discussed earlier, XRD data reveal that the Mg : Al ratio in the pure Mg : Al-LDH phases remains almost constant regardless of the reaction time, which implies that a considerable amount of the $NaAlO_2$ precursor remains unreacted in the reaction mixture. Although $NaAlO_2$ is much cheaper than a more traditional Al source (e.g. $Al(NO_3)_3$), we aimed to reuse the spent solution to promote the circular economic aspects and improve the atom efficiency. After the first synthesis, the filtrate was collected and reused in subsequent reactions by mixing it with fresh MgO microspheres in an autoclave. The XRD patterns (Fig. S6†) of the products after the 1st and 2nd cycles were identical to those collected for the material synthesised using the original synthesis protocol, demonstrating that the pure Mg/Al–CO_3 LDH phase can be obtained from spent solution. However, in the 3rd and 4th cycles, additional low-intensity diffraction peaks corresponding to the (001), (101) and (111) planes of brucite ($Mg(OH)_2$) were observed. This indicates that as the concentration of aluminium in the solution decreases with successive recycling, it eventually becomes insufficient to yield a pure Mg/Al–CO_3 LDH phase under these reaction conditions (4 h).

To investigate the effect of the Mg : Al ratio, lower concentrations of $NaAlO_2$ solutions (e.g., 0.09 M and 0.14 M) corresponding to Mg : Al ratios of 0.8 and 0.5, respectively, were employed. Extending the reaction time to 24 h and 48 h was explored to ensure equilibrium under lower $[Al^{3+}]$. XRD patterns (Fig. S7†) show that both Mg : Al input ratios resulted in a mixture of Mg/Al–CO_3 LDHs and $Mg(OH)_2$ phases regardless of the reaction time. The lattice parameters and crystallinity of the samples as listed in Table S5† indicate minor changes with increasing reaction time. The a-lattice parameter for Mg/Al–CO_3 LDHs remained constant at 0.305 nm for all samples, suggesting a consistent Mg : Al ratio in the LDH structure regardless of the aluminium concentration or reaction time. However, the c-lattice parameter decreased from 2.315 to 2.294 nm for the Mg : Al ratio of 0.5 and from 2.309 to 2.287 nm for the Mg : Al ratio of 0.8, reflecting slight adjustments in the interlayer arrangement of the carbonate anions or variations in the interlayer hydration. The crystallinity of the LDH phase improved progressively with reaction time, as observed from the increasing crystalline domain lengths in both the platelet stacking direction ($D_{(003)}$) and in the ab-plane ($D_{(110)}$), which is consistent with our earlier findings. The FT-IR spectra (Fig. S8†) confirmed the characteristic bands typical for Mg/Al–CO_3 LDHs. Moreover, a sharp and intense peak at 3699 cm^{-1} was observed, which can be assigned to the Mg–OH[44] vibrations (Fig. S7†). The N_2 adsorption–desorption isotherms and total pore volumes showed negligible variation with reaction time (Fig. S9 and Table S6†). However, with extended reaction time, the BET specific surface area increases progressively from 82 to

103 m^2 g^{-1} and from 72 to 110 m^2 g^{-1} for samples obtained with a Mg : Al ratio input of 0.5 and 0.8, respectively. This might be due to a similar Ostwald ripening effect as we previously discussed.

The obtained Mg/Al–CO_3 LDH microspheres, featuring a unique multi-hierarchical structure and high accessible surface area, show significant potential for applications in catalysis and adsorption. In this study, their capability for CO_2 capture was evaluated as a demonstration of their utility. The Mg/Al–CO_3 LDH (MgAl(x_0.2)) microspheres were calcined at 500 °C to yield the layered double oxide (LDO), MgAl(x_0.2) LDO. The MgAl(x_0.2) LDO retained its microspherical, multi-hierarchical morphology with a smaller particle size (26 ± 2.3 μm), due to shrinkage and transformation during the calcination process (Fig. 5). CO_2 adsorption isotherms were obtained under 100% CO_2 at 40 °C. The recorded adsorption isotherms (Fig. 6A) show that commercial MgO exhibits negligible CO_2 adsorption capacity, regardless of the partial pressure. In contrast, the flower-like MgO microspheres display a type II isotherm characterised by rapid adsorption at low partial pressure (monolayer adsorption) followed by gradual adsorption at higher pressure (multilayer adsorption), consistent with the mesoporous nature observed in their N_2 adsorption–desorption profiles. Similarly, the MgAl(x_0.2) microspheres exhibit analogous isotherms but show progressively higher CO_2 adsorption volume on increasing the reaction time. The total CO_2 adsorption capacity at 1 atm is summarised in Fig. 6B. The flower-like MgO microspheres exhibit an eleven-fold increase in CO_2 capture capacity compared to commercial MgO (0.33 vs. 0.03 mmol g^{-1}). This enhancement is likely attributed to the hierarchical structure of MgO microspheres, which provides a higher density of accessible surface sites, as evidenced by both N_2 adsorption–desorption measurement and CO_2-temperature programmed desorption (CO_2-TPD) (Fig. 6C). The flower-like MgO microspheres present two main CO_2 desorption features at 65 °C and 210 °C, corresponding to the presence of both weak
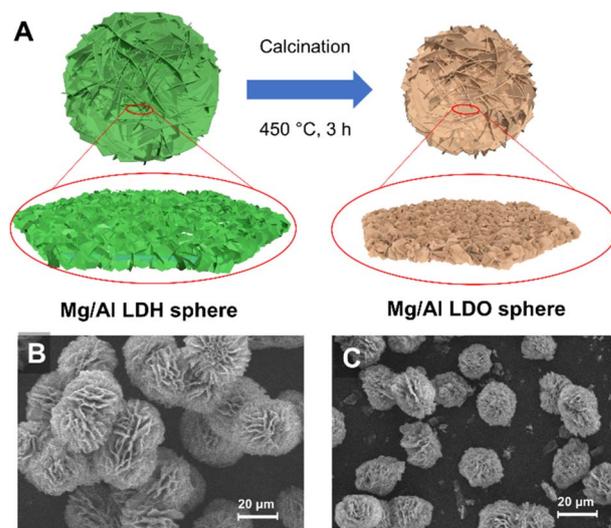

Fig. 5 (A) A schematic illustration of LDH transformation into LDO spheres and SEM images of Mg/Al LDH spheres (B) and Mg/Al LDO spheres (C).
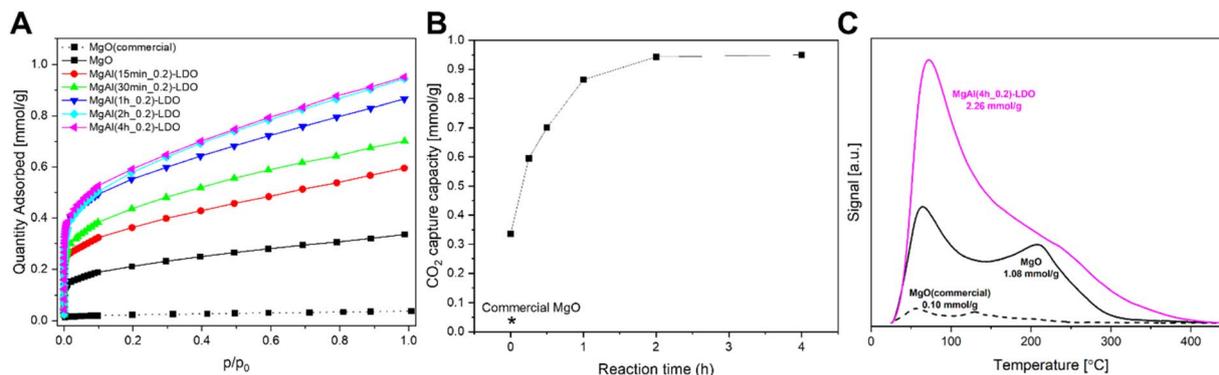
Fig. 6 (A) CO_2 adsorption isotherm for MgO and MgAl(x_0.2)-LDO samples at 40 °C; (B) CO_2 capture capacity of commercial MgO and MgAl(x_0.2)-LDO at 1 atm and 40 °C; (C) CO_2-TPD profiles of commercial MgO, flower-like MgO microspheres and MgAl(4 h_0.2)-LDO.

(OH^- groups) and medium basic sites (Mg^{2+}–O^{2-}), respectively.[6] The strong basic sites (isolated O^{2-} ions associated with cation vacancies) were not observed within the temperature range studied. In contrast, commercial MgO shows a much lower-intensity desorption feature shifted to lower temperature, indicating that the overall basic site concentration is lower and basic site strength is weaker than that of the flower-like MgO microspheres. The total number of basic sites, calculated as the amount of CO_2 desorbed from 25 to 450 °C, is over ten times higher for the flower-like MgO microspheres than for commercial MgO (1.08 vs. 0.10 mmol g^{-1}, respectively). The basic site density is also significantly higher in the spherical MgO microspheres (10.69 and 3.85 mmol g^{-1}). These results suggest that the enhanced basicity of the flower-like MgO microspheres is due to their multi-hierarchical morphology which increases the accessibility of basic sites. For the MgAl(x_0.2) series, CO_2 capture efficiency increased with the Mg_xAl phase content, reaching a plateau for samples derived from the pure Mg/Al–CO_3 LDH phase synthesised over 2 h. These samples achieved a CO_2 adsorption capacity of approximately 0.95 mmol g^{-1}, (1 atm CO_2), which is 2.8 times higher than that for the flower-like MgO microspheres. Adsorption capacities at lower CO_2 concentrations were 0.56 mmol g^{-1} at 0.15 atm CO_2, and 0.21 mmol g^{-1} at 400 ppm CO_2. When a MgAl(x_0.2) sample, prepared from a recovered $NaAlO_2$ solution, was tested for CO_2 adsorption, it exhibited identical behaviour to the first batch. The enhanced CO_2 uptake of Mg_xAl-LDO materials is related to their bi-hierarchical structure which makes more basic sites available for CO_2 adsorption. This is confirmed by the CO_2-TPD measurement. The CO_2-TPD profile recorded for MgAl(4 h_0.2)-LDO exhibits a highly intense low-temperature peak at 70 °C and a broad shoulder in the higher temperature regions with a flex point at around 230 °C. The total number of basic sites was determined to be 2.26 mmol g^{-1}, which is 2.1 times higher than that for the parent MgO.

Conclusions

In this study, we successfully synthesised Mg/Al–CO_3 LDH microspheres with a unique multi-hierarchical structure, demonstrating significant advancements in material design and functionality with high accessible surface area and porosity. The transformation of flower-like MgO microspheres into Mg/Al–CO_3 LDHs through a hydrothermal reaction with $NaAlO_2$ was systematically studied. When a Mg : Al input ratio of 0.2 was applied, the LDH phase was observed within 15 minutes of the reaction which diminishes and ultimately disappears after 2 h. The spent aluminium-containing solution can be reused at least twice for pure LDH formation from MgO, further aligning this process with principles of circular economy and sustainable material synthesis. A lower concentration of $NaAlO_2$ (e.g. 0.09 M and 0.14 M) results in a mixture of both Mg_xAl–CO_3 LDH and $Mg(OH)_2$ phases regardless of the reaction time or $NaAlO_2$ concentration. The hierarchical Mg/Al–CO_3 LDH derived LDO microspheres exhibited excellent CO_2 adsorption capacities, significantly outperforming commercial MgO (32-fold) and flower-like MgO microspheres (2.8-fold). This enhanced performance was attributed to the unique multi-hierarchical structure which promotes an increased number of accessible basic sites for CO_2 adsorption. The developed multi-hierarchical Mg/Al–CO_3 LDH microspheres show immense potential for applications in catalysis and adsorption technologies. The synthesis protocol and material properties established in this work provide a strong foundation for the further development of advanced multifunctional materials tailored for environmental and industrial applications.

Experimental

Synthesis of MgO(p) microspheres

25 mL of aqueous solutions of 1 M magnesium chloride (Sigma-Aldrich, ≥98%, anhydrous) and sodium carbonate (Sigma-Aldrich, ≥99.5%) were prepared separately. Then both solutions were pre-heated in an oven for 15 minutes to 80 °C. Subsequently, the Na_2CO_3 solution was added dropwise (10.5 mL min^{-1}) to the $MgCl_2$ solution at 80 °C. After precipitation, the milky solution was aged without stirring in the oven for 2 h at 80 °C. After this time, the hot white precipitate was filtered, washed with deionised water (to get pH = 7) and dried in a vacuum at 30 °C overnight.

Synthesis of MgO microspheres

The MgO precursor (MgO(p)) was calcined at 500 °C for 3 h (heating rate 2 °C min^{-1}) in a muffle furnace in static air.

Synthesis of microspherical MgAl–CO$_3$ LDHs

Typically, a 0.35 M aqueous solution of sodium aluminate was prepared by dissolving 1.017 g of NaAlO$_2$ (Sigma-Aldrich, technical grade) in 35 mL of DI water. The solution was heated in an oven to 80 °C and then poured into a Teflon-lined stainless-steel autoclave. 100 mg of calcined MgO was then placed inside the autoclave, and sealed and heated at 80 °C for various periods of time (from 15 minutes to 48 h). After this time, the autoclave was cooled under cold running water, and the solid product was filtered, washed, and dried under vacuum at 30 °C overnight. The collected samples were denoted as MgAl(x_0.2), where x is the time of the hydrothermal reaction (15 min, 30 min, 1 h, 2 h, 4 h, 24 h, and 48 h), while 0.2 is the Mg : Al ratio in the reaction mixture (input).

Alternatively, the above synthesis procedure was performed using 0.09 M and 0.14 M NaAlO$_2$ solution, which corresponded to Mg : Al input ratios of 0.8 and 0.5, respectively. These samples were denoted as MgAl(x_y), where x is the synthesis time (4 h, 24 h, and 48 h) and y is the Mg/Al ratio in the input.

Synthesis of microspherical MgAl LDO

The LDO samples were obtained by calcining the corresponding LDH samples in a crucible at 450 °C for 3 h (heating rate 5 °C min^{-1}) in a muffle oven under static air.

Data availability

All the data supporting the findings of this study are available within the article, its ESI† or from the corresponding authors upon request.

Author contributions

T. Kondratowicz performed the experimental work and conceptualised the research; C. Besnard and J.-C Tan assisted with the cross-sectional electron microscopy studies; C. Chen supervised the research; D. O'Hare conceptualised and supervised the research and acquired the funding. C. Chen, T. Kondratowicz, R. Turnell-Ritson and D. O'Hare wrote the paper, and all authors discussed the results and edited the manuscript.

Conflicts of interest

There are no conflicts to declare.

Acknowledgements

Notes and references

1 F. Cavani, F. Trifirò and A. Vaccari, *Catal. Today*, 1991, **11**, 173–301.

2 V. Rives, *Layered Double Hydroxides: Present and Future*, Nova Publishers, 2001.

3 P. Zhang, T. He, H. Chen, P. Li, M. Xiang, N. Ding and S. Deng, *J. Colloid Interface Sci.*, 2020, **578**, 124–134.

4 J. Yu, K. Ruengkajorn, D.-G. Crivoi, C. Chen, J.-C. Buffet and D. O'Hare, *Nat. Commun.*, 2019, **10**, 2398.

5 D. J. Leung, K. R. Laney, P. Kenyon, N. H. Rees, J.-C. Buffet, C. Chen and D. O'Hare, *Dalton Trans.*, 2024, **53**, 6200–6206.

6 M. Bolognini, F. Cavani, D. Scagliarini, C. Flego, C. Perego and M. Saba, *Catal. Today*, 2002, **75**, 103–111.

7 G. Fan, F. Li, D. G. Evans and X. Duan, *Chem. Soc. Rev.*, 2014, **43**, 7040–7066.

8 C. Chen, P. Gunawan and R. Xu, *J. Mater. Chem.*, 2011, **21**, 1218–1225.

9 J. Hu, X. Tang, Q. Dai, Z. Liu, H. Zhang, A. Zheng, Z. Yuan and X. Li, *Nat. Commun.*, 2021, **12**, 3409.

10 C. Del Hoyo, *Appl. Clay Sci.*, 2007, **36**, 103–121.

11 Q. Wang and D. O'Hare, *Chem. Rev.*, 2012, **112**, 4124–4155.

12 Q. Wang and D. O'Hare, *Chem. Commun.*, 2013, **49**, 6301–6303.

13 C. Chen, A. Wangriya, J.-C. Buffet and D. O'Hare, *Dalton Trans.*, 2015, **44**, 16392–16398.

14 C. Chen, M. Yang, Q. Wang, J.-C. Buffet and D. O'Hare, *J. Mater. Chem. A*, 2014, **2**, 15102–15110.

15 V. Erastova, M. T. Degiacomi, D. O'Hare and H. C. Greenwell, *RSC Adv.*, 2017, **7**, 5076–5083.

16 C. Chen, R. Felton, J.-C. Buffet and D. O'Hare, *Chem. Commun.*, 2015, **51**, 3462–3465.

17 C. Chen, C. F. Byles, J.-C. Buffet, N. H. Rees, Y. Wu and D. O'Hare, *Chem. Sci.*, 2016, **7**, 1457–1461.

18 P. Gunawan and R. Xu, *Chem. Mater.*, 2009, **21**, 781–783.

19 Z. Li, X. Zhang, Y. Kang, C. C. Yu, Y. Wen, M. Hu, D. Meng, W. Song and Y. Yang, *Adv. Science*, 2021, **8**, 2002631.

20 M. Shao, F. Ning, J. Zhao, M. Wei, D. G. Evans and X. Duan, *J. Am. Chem. Soc.*, 2012, **134**, 1071–1077.

21 C. Chen, R. Felton, J.-C. Buffet and D. O'Hare, *Chem. Commun.*, 2015, **51**, 3462–3465.

22 T. Kondratowicz, S. Slang, L. Dubnová, O. Kikhtyanin, P. Bělina and L. Čapek, *Appl. Clay Sci.*, 2022, **216**, 106365.

23 Z. Li, S. Mao, Y. Yang, Z. Sun and R. Zhao, *J. Colloid Interface Sci.*, 2021, **585**, 85–94.

24 J. Zhang, X. Xie, C. Li, H. Wang and L. Wang, *RSC Adv.*, 2015, **5**, 29757–29765.

25 H. Zhong, T. Liu, S. Zhang, D. Li, P. Tang, N. Alonso-Vante and Y. Feng, *J. Energy Chem.*, 2019, **33**, 130–137.

26 M. Shao, F. Ning, J. Zhao, M. Wei, D. G. Evans and X. Duan, *Adv. Funct. Mater.*, 2013, **23**, 3513–3518.

27 S. Purwajanti, L. Zhou, Y. Ahmad Nor, J. Zhang, H. Zhang, X. Huang and C. Yu, *ACS Appl. Mater. Interfaces*, 2015, **7**, 21278–21286.

28 L. Min, J. Duan, L. Liu, S. Ge, W. Zhang and Y. Wang, *Dalton Trans.*, 2022, **51**, 2033–2040.

29 A. Botha and C. A. Strydom, *Hydrometallurgy*, 2001, **62**, 175–183.

30 P. Kristova, L. J. Hopkinson, K. J. Rutt, H. M. A. Hunter and G. Cressey, *Appl. Geochem.*, 2014, **50**, 16–24.

31 Y. Xiong and A. S. Lord, *Appl. Geochem.*, 2008, **23**, 1634–1659.

32 Q. Chen, T. Hui, H. Sun, T. Peng and W. Ding, *Open Chem.*, 2020, **18**, 951–961.

33 P. Ballirano, C. De Vito, S. Mignardi and V. Ferrini, *Chem. Geol.*, 2013, **340**, 59–67.

34 C. Barad, G. Kimmel, A. Opalińska, S. Gierlotka and W. Łojkowski, *Heliyon*, 2024, **10**, e31275.

35 J. J. Creasey, A. Chieregato, J. C. Manayil, C. M. A. Parlett, K. Wilson and A. F. Lee, *Catal. Sci. Technol.*, 2014, **4**, 861–870.

36 O. Kikhtyanin, L. Čapek, L. Smoláková, Z. Tišler, D. Kadlec, M. Lhotka, P. Diblíková and D. Kubička, *Ind. Eng. Chem. Res.*, 2017, **56**, 13411–13422.

37 C. V. Luengo, M. A. Volpe and M. J. Avena, *J. Environ. Chem. Eng.*, 2017, **5**, 4656–4662.

38 M. Thommes, K. Kaneko, A. V. Neimark, J. P. Olivier, F. Rodriguez-Reinoso, J. Rouquerol and K. S. W. Sing, *Pure Appl. Chem.*, 2015, **87**, 1051–1069.

39 C. Besnard, A. Marie, P. Buček, S. Sasidharan, R. A. Harper, S. Marathe, K. Wanelik, G. Landini, R. M. Shelton and A. M. Korsunsky, *Mater. Des.*, 2022, **220**, 110829.

40 S. Jin, K.-J. Ko, Y.-G. Song, K. Lee and C.-H. Lee, *Chem. Eng. J.*, 2019, **359**, 285–297.

41 P. Kenyon, S. Roberts, Z. R. Turner, N. H. Rees and D. O'Hare, *J. Phys. Chem. C*, 2024, **128**, 12249–12258.

42 S. Miyata, *Clays Clay Miner.*, 1983, **31**, 305–311.

43 S. Kandula, K. R. Shrestha, G. Rajeshkhanna, N. H. Kim and J. H. Lee, *ACS Appl. Mater. Interfaces*, 2019, **11**, 11555–11567.

44 M. H. Zahir, M. M. Rahman, K. Irshad and M. M. Rahman, *Nanomaterials*, 2019, **9**, 1733.